Simulated Impact of Ocean Alkalinity Enhancement on Atmospheric CO_2 Removal in the Bering Sea

Hongjie Wang[1] , Darren J. Pilcher[2,3] , Kelly A. Kearney[2,4] , Jessica N. Cross[3], O. Melissa Shugart[5], Matthew D. Eisaman[6], and Brendan R. Carter[2,3]

[1]Graduate School of Oceanography, University of Rhode Island, Narragansett, RI, USA, [2]Cooperative Institute for Climate, Ocean, and Ecosystem Studies, University of Washington, Seattle, WA, USA, [3]Pacific Marine Environmental Laboratory, National Oceanic and Atmospheric Administration, Seattle, WA, USA, [4]Alaska Fisheries Science Center, National Oceanic and Atmospheric Administration, Seattle, WA, USA, [5]Department of Chemistry and Biochemistry, University of South Carolina, Columbia, SC, USA, [6]Department of Electrical and Computer Engineering, Stony Brook University, Stony Brook, NY, USA

Abstract Ocean alkalinity enhancement (OAE) has the potential to mitigate ocean acidification (OA) and induce atmospheric carbon dioxide (CO_2) removal (CDR). We evaluate the CDR and OA mitigation impacts of a sustained point-source OAE of 1.67×10^{10} mol total alkalinity (TA) yr^{-1} (equivalent to 667,950 metric tons NaOH yr^{-1}) in Unimak Pass, Alaska. We find the alkalinity elevation initially mitigates OA by decreasing pCO_2 and increasing aragonite saturation state and pH. Then, enhanced air-to-sea CO_2 exchange follows with an approximate *e*-folding time scale of 5 weeks. Meaningful modeled OA mitigation with reductions of >10 µatm pCO_2 (or just under 0.02 pH units) extends 100–100,000 km^2 around the TA addition site. The CDR efficiency (i.e., the experimental seawater dissolved inorganic carbon (DIC) increase divided by the maximum DIC increase expected from the added TA) after the first 3 years is 0.96 ± 0.01, reflecting essentially complete air-sea CO_2 adjustment to the additional TA. This high efficiency is potentially a unique feature of the Bering Sea related to the shallow depths and mixed layer depths. The ratio of DIC increase to the TA added is also high (≥ 0.85) due to the high dissolved carbon content of seawater in the Bering Sea. The air-sea gas exchange adjustment requires 3.6 months to become (>95%) complete, so the signal in dissolved carbon concentrations will likely be undetectable amid natural variability after dilution by ocean mixing. We therefore argue that modeling, on a range of scales, will need to play a major role in assessing the impacts of OAE interventions.

Plain Language Summary The Intergovernmental Panel on Climate Change suggests that carbon dioxide (CO_2) removal (CDR) approaches will be required to stabilize the global temperature increase at 1.5–2°C. In this study, we simulated the climate mitigation impacts of adding alkalinity (equivalent to 667,950 metric ton NaOH yr^{-1}) in Unimak Pass on the southern boundary of the Bering Sea. We found that adding alkalinity can accelerate the ocean CO_2 uptake and storage and mitigate ocean acidification near the alkalinity addition. It takes about 3.6 months for the Ocean alkalinity enhancement impacted area to take up the extra CO_2. The naturally cold and carbon rich water in the Bering Sea and the tendency of Bering Sea surface waters to linger near the ocean surface without mixing into the subsurface ocean both lead to high CDR efficiencies (>96%) from alkalinity additions in the Bering Sea. However, even with high efficiency, it would take >8,000 alkalinity additions of the kind we simulated to be operating by the year 2100 to meet the target to stabilize global temperatures within the targeted range.

1. Introduction

The Intergovernmental Panel on Climate Change (IPCC) suggests that intentional carbon dioxide (CO_2) removal (CDR) approaches will be required to stabilize global atmospheric temperatures at 1.5–2°C above the preindustrial baseline (IPCC, 2022). IPCC analysis suggests that we will need to extract 5.5 GT CO_2 per year out of the atmosphere by 2100 to limit global warming to 1.5°C (IPCC, 2022). This CDR will mostly offset legacy emissions and emissions that cannot be avoided. The ocean is a promising geochemical reservoir for CDR because it contains ~45 times more carbon than the atmosphere, and acts as a key control for natural atmospheric CO_2 concentrations. The ocean has taken up 30% of anthropogenic emissions to date (Friedlingstein et al., 2020). Storage of dissolved anthropogenic CO_2 has increased the H^+ concentrations and decreased the carbonate ion (CO_3^{2-}) concentrations in the ocean in a process known as ocean acidification (OA, Orr et al., 2005). OA has a significant

and lasting impact on marine organisms, as acidified water can induce shell dissolution in ecologically and economically important organisms, decrease filtration and feeding behavior in shellfish, and alter phytoplankton community structure (Bednaršek et al., 2021; Doney et al., 2020; Grear et al., 2017; Kleypas et al., 2019; Meseck et al., 2020). Accordingly, the oceans are likely to play an important role in any CDR strategy that operates at the required scale, yet any ocean CDR approach must also be weighed by whether it exacerbates or ameliorates OA.

The National Academies of Science ocean-based CDR research plan (National Academies of Sciences, Engineering, and Medicine, 2021) suggests that ocean alkalinity enhancement (OAE) is a promising CDR approach that needs additional research. This approach aims to increase the large natural ocean carbon storage (~40,000 PgC, Falkowski et al., 2000) that results from the high total alkalinity (TA) of seawater. Seawater TA allows CO_2 dissolved in the ocean to be stored as abundant and stable carbonate and bicarbonate ions. On long timescales (~100–200 ka), elevated weathering from higher atmospheric CO_2 levels is expected to increase ocean TA and thereby increase the tendency of the ocean to absorb CO_2 from the atmosphere. This will ultimately reduce atmospheric CO_2 to values close to preindustrial (Renforth & Henderson, 2017). OAE approaches work by either accelerating mineral weathering or by otherwise adding TA to the sea surface to speed up this feedback. A significant challenge for OAE approaches is how to speed TA increases enough for them to be relevant on the timescales needed to meet carbon targets (decades to centuries).

Strategies for increasing seawater TA include electrochemical acid removal (National Academies of Sciences, Engineering, and Medicine, 2021; Rau, 2008) and accelerating weathering of alkaline minerals on land (Caldeira & Rau, 2000; Harvey, 2008; Kheshgi, 1995; Kohler et al., 2010; Rau, 2011; Rau & Caldeira, 1999; Rau et al., 2013; Renforth & Henderson, 2017; Schuiling & Krijgsman, 2006). Both approaches to OAE have the potential to ameliorate OA's effects by directly increasing CO_3^{2-} in the ocean. This OA mitigation effect is expected to wane over the 1–12 months required for sea-air CO_2 equilibration (Jones et al., 2014) due to elevated ocean carbon uptake with the net reaction:

$$CO_2 + H_2O + CO_3^{2-} \leftrightarrow 2HCO_3^-$$

At present, OAE approaches are in the very early phases of development and require testing for effectiveness, efficiency, and ecological risk. Earth system models have simulated idealized alkalinity additions globally or on a wide patch of the surface ocean (Burt et al., 2021; Ferrer-González & Ilyina, 2016; Ilyina et al., 2013; Keller et al., 2014). These models reveal the potential of TA enhancement to mitigate atmospheric CO_2 and OA. Burt et al (2021) further showed the regional responses to OAE vary depending upon the background concentrations of dissolved inorganic carbon (DIC) and TA. They showed that adding alkalinity to the Southern Ocean resulted in the highest carbon-uptake efficiency—defined in their study as the moles of atmospheric CO_2 removed per mol of alkalinity added—of the regions they considered, sequestering 12% more carbon than a globally-uniform TA addition experiment. Relatedly, Butenschön et al. (2021) examine the impacts of alkaline mineral additions across the Mediterranean and show that such an approach could meaningfully reduce or reverse regional OA. These models simulated a TA enhancement over a wide area, consistent with idealized enhanced mineral dispersal and dissolution over a broad area. However, modeling a sustained point source is important for OAE induced by electrochemical acid extraction, since these facilities will likely be located on the coast, powered by the electrical grid, and use existing outfall pipes for alkalinity dispersal.

It is common to refer to the observed ratio of the excess simulated DIC to the TA added as the efficiency of an OAE effort, but we note that this is the result of two combined terms: The first term has to do with the expected CDR that would result from a TA addition given infinite opportunity for air-sea exchange, which we refer to as the "CDR potential" or $CDR_{Potential}$. The mole ratio between the $CDR_{potential}$ and the TA addition is less than 1:1 everywhere in the ocean and varies depending upon the properties of the seawater (e.g., the temperature, salinity, and the buffer factor). The second term reflects the degree to which the modified seawater has had an opportunity for air-sea gas exchange and therefore had a chance to realize its potential impact. We contend the second term is more rightly called an efficiency because it reflects a loss in potential function, whereas the first is a ratio inherent to the process. We therefore call the first term the "TA addition potential impact ratio," the second term the "CDR efficiency," and their product the simulated or observed "CDR impact ratio." Air-sea gas exchange is expected to continue until the TA addition is fully offset by enhanced ocean CO_2 storage, so the CDR efficiency and the simulated CDR impact ratio are both expected to increase over time until the efficiency reaches ~1. This

timescale is important to consider for "ton year" CDR calculations because the CDR impact of a TA addition will vary over time.

Here we build upon past research using a TA addition simulation in the Bering Sea that is intended to represent a hypothetical large-scale electrochemical acid extraction CDR intervention near Unimak Pass, Alaska. Our aims with this analysis of this TA addition are three-fold: (a) to quantify the CDR impact; (b) to assess the CDR efficiency on timescales of several years; and (c) to quantify the regional OA-mitigation footprint. While the CDR efficiency in the Bering Sea has not been assessed previously to our knowledge, the seawater conditions that favored high CDR impact in the Southern Ocean in the study by Burt et al. (2021) are also found in the Bering Sea: specifically, there is a naturally-high water column DIC:TA ratio in the surface ocean. Multiple factors can further maximize the responses of OAE in the Bering Sea, similar to the different factors that control sea-air gas exchange in other settings. For example, the drawdown of atmospheric CO_2 after the addition of alkalinity can require months or more to equilibrate, so extended contact of alkalinity-enhanced surface waters with the atmosphere improves CDR efficiencies on short timescales. Unlike the Southern Ocean, the Bering Sea is dominated by a shallow continental shelf, and there are no known deep or intermediate water masses formed along the Bering shelf. These features should help ensure the perturbed seawater with elevated TA has sufficient contact with the atmosphere to approach a new equilibrium before entering the ocean interior, likely resulting in a high CDR efficiency. The Bering Sea is also considered especially vulnerable to OA (Cross et al., 2014) making the Bering Sea a natural laboratory for examining the effects of the OAE on CO_2 removal and OA amelioration. Thus, we use the Bering Sea as a case study to test whether this strategy can be useful for regional OA mitigation.

2. Methodology

2.1. Study Area

The Bering Sea is located between Russia and Alaska, extending from the Aleutian Islands north to the Bering Strait (Figure 1). It consists of a narrow western shelf, deep central basin, and wide eastern shelf. The eastern Bering Sea shelf stretches >500 km from the coast of Alaska to the continental shelf break, is relatively flat with a maximum depth of 180 m at the shelf break (Stabeno et al., 2016), and consists of three domains with distinct mixing characteristics. The coastal domain (depth <50 m) is well-mixed seasonally; the middle domain is seasonally stratified with a wind-mixed surface layer (depth 15–40 m) and tidally mixed lower layers (depth below 40 m). The outer-shelf domain (depth 100–200 m) has a wind-mixed surface layer and a tidally mixed bottom layer separated by an intermediate layer (Hunt & Stabeno, 2002). The mixed layer depth in the eastern Bering shelf is generally shallower than 50 m across all three domains. Approximately half the water on the eastern shelf originates from water flowing from the Gulf of Alaska through Unimak Pass (Aagaard et al., 2006). Geostrophic transport on the shelf is northward with an average 0.25 Sv in the warm months to 0.43 Sv in the cold months. Much of the transport occurs along the 50 and 100 m isobaths. Transport along 100 isobath is more than twice that along the 50 m isobath, and together they account for half of the transport through the Bering Strait (Stabeno et al., 2016). A typical transit time from Unimak Pass to the Bering Strait is around 13 months (Stabeno et al., 2016). The Pacific Water (PW) from Unimak Pass is naturally cold and DIC rich. The additional seasonal respiration of terrestrial and marine organic matter together contribute additional DIC to these water masses, yielding persistently low pH and, at times, conditions that are corrosive for carbonate minerals across the Bering Sea (Cross et al., 2018).

2.2. Model Design and TA Addition

In this study, we use a regional ocean model known as Bering10K. Bering10K is an implementation of the Regional Ocean Modeling System (ROMS), a free-surface, primitive equation hydrographic model (Haidvogel et al., 2008; Shchepetkin & McWilliams, 2005). The Bering10K model grid spans the Bering Sea and northern Gulf of Alaska, with approximately 10-km horizontal resolution and 30 terrain-following depth levels (Hermann et al., 2016; Kearney et al., 2020). Bering10K includes ecosystem processes via the BESTNPZ model, which simulates biological processes linking multiple nutrient, phytoplankton, and zooplankton functional groups as well as benthic and sympagic (ice) ecosystem components (Gibson & Spitz, 2011; Kearney et al., 2020). Carbonate chemistry is implemented as described in Pilcher et al. (2019) by adding two additional tracers (DIC and TA) to calculate the full marine carbonate system through the OCMIP-2 protocols (Orr et al., 1999) and CO2SYS (Lewis
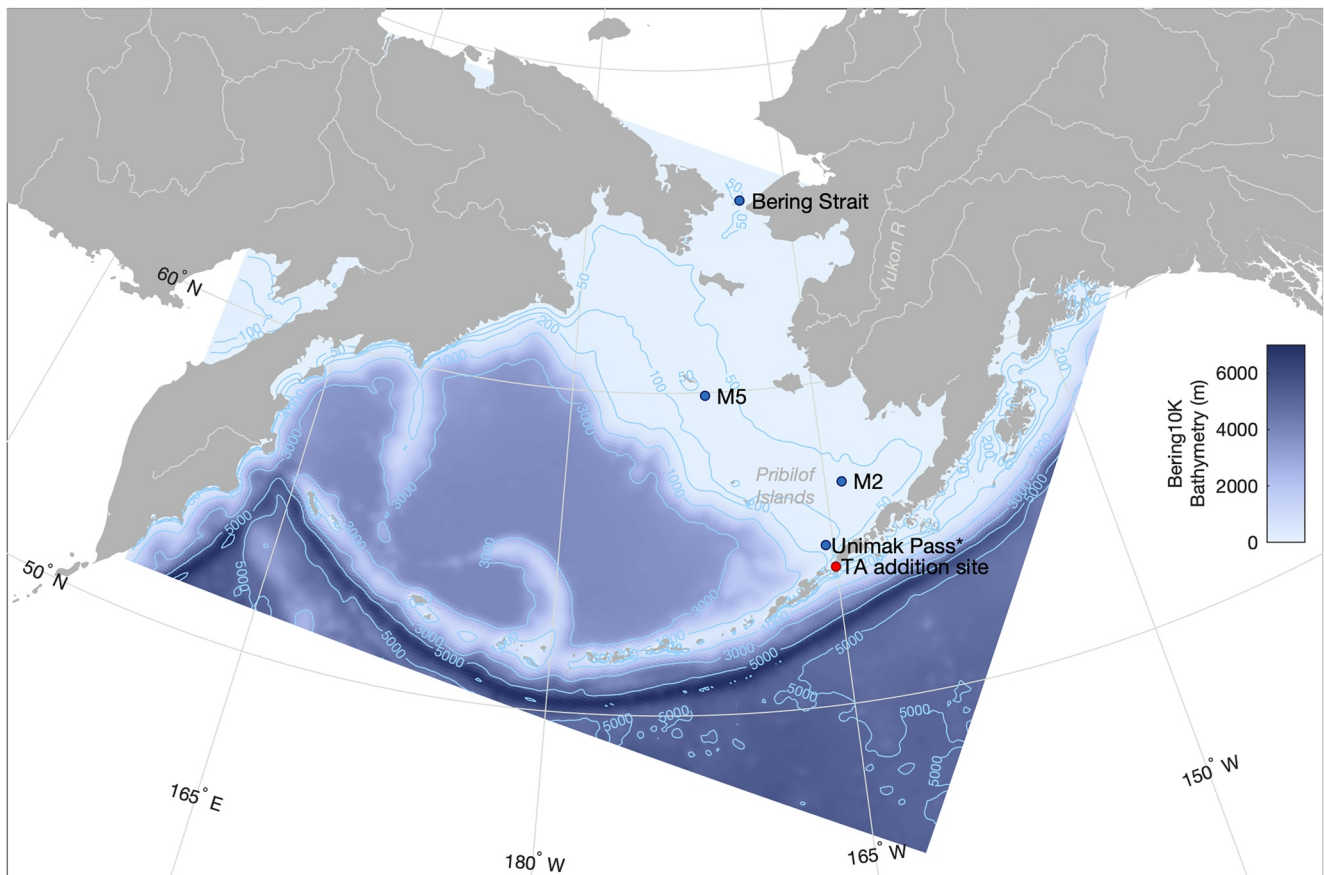
Figure 1. The model domain in this study with the total alkalinity (TA) addition site in Unimak Pass (red circle) and four simulated "stations" (i.e., specific grid cells within the model) that we consider in greater detail (blue circles): Unimak Pass* (60 km northeast of the TA addition site), M2 (56.87°N, 164.05°W), M5 (59.9°N, 171.7°W), and the Bering Strait. The M2 and M5 simulated stations are chosen to match long-term moored observing platforms of the same names along the 70-m isobath (Stabeno et al., 2016).

et al., 1998). Model sea-air CO_2 exchange is calculated through the sea-air ΔpCO_2 and the wind speed following Wanninkhof (2014). Bering10K also includes a sea ice model, with the presence of sea ice decreasing the magnitude of air-sea fluxes proportional to the fraction of a grid cell covered. Rigorous skill assessment has been done previously for carbonate system variables in the Bering10K model by Pilcher et al. (2019), and the Bering10K model is skillful in predicting mean-state conditions, particularly near the surface.

Two simulations were run for this study: a control and an experimental simulation. Both simulations are variants on the hindcast simulation used for many previous Bering10K-based studies; atmospheric and lateral boundary conditions for the hindcast are derived from reanalysis datasets (primarily the Climate Forecast System Operational Analysis (Saha et al., 2010) for the time period of interest for this current study). Forcing also includes freshwater and carbonate system inputs from rivers, based on observational data from the mouth of the Yukon River. Northern boundary transport is one-way through Bering Strait and is relaxed to 0.8 Sv based on observational evidence (Woodgate & Aagaard, 2005). Further details of this model configuration, including thorough validation of the physics, primary production, and carbonate dynamics, can be found in previous publications (Hermann et al., 2016; Kearney et al., 2021, 2020; Pilcher et al., 2019). For the control, we ran a 10-year simulation, repeating the same 2020 boundary forcing—including atmospheric pCO_2—for each year. We chose to repeat the forcing in order to capture realistic seasonality but limit interannual variations; 2020 was chosen as a recent year with an average amount of sea ice. The TA addition experiment is identical to the control except for an additional surface flux of TA.

It should be noted that the feedbacks between the ocean and ecosystem components and the carbonate system within the Bering10K model are unidirectional. In the model, there are no direct or indirect feedbacks from the

carbonate variables (DIC and TA) on any physical or ecosystem state variables. Therefore, differences between the control and OAE simulations profiled here can be attributed purely to OAE and the passive advection and diffusion of the elevated TA plume away from the surface at Unimak Pass. While there is evidence for biogeo-chemical feedbacks on the Bering Sea shelf (Cross et al., 2013) that could introduce additional complexity in the real world, our focus here is to isolate and simulate the direct impact of OAE as a first-order approach.

The TA addition is applied as a continuous flux across the surface boundary into a single grid cell located in the middle of Unimak Pass, at a rate of 4 µmol m^{-2} s^{-1} (equivalent to 13.8 tons of NaOH per km^2 per day). The TA addition starts from January of Year 1 (following a ~50 years hindcast) and continues for 10 years. The grid cell surface area for this cell is 132 km^2, so the overall domain-wide TA addition rate is 1.67×10^{10} mol yr^{-1} (equivalent to 667,950 tons of NaOH per year). Previously published laboratory results on bipolar membrane electrodialysis systems (de Lannoy et al., 2018; Eisaman, 2020; Eisaman et al., 2012, 2018; Sabatino et al., 2020) and recent measurements suggest an electricity requirement of 1.8–2.3 MWh/tCO_2 for the range $0.9 \geq$ sea-air CO_2 flux/TA addition ≥ 0.7. This simulated TA addition is intended to be consistent with a plausible large-scale facility consuming ~1 TWh each year, which could be powered by around 30 8 MW offshore wind turbines, assuming at least 50% of the power generated can be effectively used by the systems.

To remain net carbon negative, the electrical source for this implementation needs to have a sufficiently low carbon footprint. This could be achieved through the application of wind energy: a carbon intensity of 0.012 t(CO_2)/MWh typical for wind-generated electricity results in CO_2 emissions equal to only 2.5% of laboratory-derived estimates of the CO_2 capture rate, while traditional fossil energy sources would offset a much larger percentage of the CO_2 captured. In addition, this method also generates tons of dilute hydrochloric acid as a byproduct of the TA generation (the exact amount depends on the acid concentration), and this product must offset other HCl produc-tion, be neutralized, or be sequestered if the intervention is to result in net CDR. While the volumes of co-product acid would be significant, this opens up the possibility for entirely new uses for carbon-neutral, low-cost acid such as enhanced mineral recovery (Hamilton et al., 2020; Scott et al., 2021), fertilizer production (Schorr et al., 2010), biomass processing (Perotto et al., 2018), enhancement of CO_2 mineralization kinetics (Kelemen et al., 2019), or the neutralization of toxic alkaline waste streams (Qi, 2021). These challenges and opportunities are noted for perspective, and are not the topic of this research. While this study is motivated by research into this electrodial-ysis technique, the scientific outcomes will also be applicable for other point-source OAE methods.

2.3. Analysis Metrics

In this study, we use " ′ " to refer to the differences between the experimental and control simulation values (experimental minus control). Unlike global ocean models (e.g., Burt et al., 2021), regional models lose tracers through mixing across lateral boundaries. Therefore we cannot use the ratio of domain integrated DIC′ and TA′ as a metric for the CDR impact ratio of a given TA addition. Fortunately, as we later show, the enhanced flux of CO_2 into the ocean, SAF′ (with our positive values indicating additional CO_2 going into the ocean), seems to be located almost entirely within the boundaries of our modeled domain. We can therefore compare the total amount of simulated TA addition for a span of time (TA$^+$) to the SAF′ integrated spatially across the modeled domain and temporally over the same time span (SAF$^+$) as a metric for the CDR achieved per unit TA added (which is the first metric that we aim to quantify). One problem with this metric is that the SAF′ responds more slowly than the TA′. However, we show that this metric, when calculated on an annual basis, reaches a steady state within our model domain after several years. Thus, we can rely upon these steady state values for an indication of the longer-term CDR from a TA addition. Defined in this fashion, the SAF$^+$/TA$^+$ is:

$$\text{SAF}^+/\text{TA}^+ = \sum_{i=1}^{182} \sum_{j=1}^{258} \frac{\sum_{t=1}^{366} F\text{CO}_{2'i,j,t} \times \text{Area}_{i,j}}{\text{Annual TA Addition}}$$

where $F\text{CO}_{2'i,j,t}$ is the sea-air CO_2 flux difference at each grid cell i, j at time t in mmol m^{-2} d^{-1}. $\text{Area}_{i,j}$ is the area (m^2) in each grid i,j. The annual $F\text{CO}_2'$ is integrated over 366 days (2020 is a leap year). The annual TA addition is a constant: 1.67×10^{10} mol yr^{-1}.

To define the CDR efficiency ($\text{CDR}_{\text{efficiency}}$), we first quantify $\text{CDR}_{\text{Potential}}$ as the maximum DIC′ expected from the seawater chemistry change that results from the OAE:

$$\text{CDR}_{\text{potential}} = \text{DIC}_{\text{eq}} - \text{DIC}_{\text{control}}$$

DIC$_{eq}$ is calculated from the TA in the experimental simulation and the pCO$_2$ from the control simulation, and therefore represents the DIC expected for seawater with elevated TA and in the air-sea equilibrium state observed in the control run. The CDR efficiency is then estimated as the ratio of the simulated DIC′ to the CDR$_{Potential}$ when these two properties are summed across the entire model domain:

$$\text{CDR}_{\text{efficiency}} = \frac{\sum_{i=1}^{182} \sum_{j=1}^{258} \sum_{l=1}^{30} \overline{\text{DIC}'_{,i,j,l} \times V_{i,j,i}}}{\sum_{i=1}^{182} \sum_{j=1}^{258} \sum_{l=1}^{30} \overline{\text{CDR}_{\text{potential},i,j,l} \times V_{i,j,l}}}$$

Here $\overline{\text{DIC}'_{,i,j,l}}$ is the annual mean DIC difference between OAE and control experiments at grid cell i, j, and depth l. $\overline{V_{,i,j,l}}$ is bin volume at grid i, j and depth l.

There are three caveats for the CDR$_{\text{efficiency}}$ calculation that all individually suggest the metric should be thought of as a lower bound estimate for the value that would be estimated from a global-domain model or a model that also simulates cessation of the TA source. First, as with the SAF$^+$/TA$^+$ calculation, the loss of tracers at the model domain boundary means we fail to account for the (thought to be minimal) SAF′ that would occur outside of the model domain. Second, the DIC′ inventory will always lag the TA′ inventory when there is an ongoing TA′ addition within the modeled domain because there will always be TA′ that has not yet had a chance to induce DIC′ storage. Unlike the comparison between the SAF$^+$ and TA$^+$, which are both rates, this remains true at steady state. This is also true for global models, but can be circumvented by continuing the simulation after the end of the simulated TA′. Mitigating this, we show that the time required to reach steady state is long compared to the time required for air-sea gas exchange in our model, and thus it is reasonable to expect that most of the TA′ in the domain at steady state has had an opportunity to induce DIC′ storage. Finally, in most places in the ocean, the subsurface pCO$_2$ is greater than the pCO$_2$ at the surface where sea-air exchange takes place, so this formulation might slightly over-estimate the expected DIC′ and underestimate the calculated efficiency. To address this third caveat, we note that the alternate formulation using the atmospheric pCO$_2$ of 410 μatm in place of the simulated pCO$_2$ yields similar results in this study because the TA′ is typically found near the surface in these simulations. We note this complication primarily as a caution for future studies that may have more entrainment of TA′ into the ocean interior. For discussion purposes, we define the "unrealized CDR$_{\text{Potential}}$" as the difference between the CDR$_{\text{Potential}}$ and DIC′, or the difference between the potential and simulated CDR impacts.

3. Results and Discussion

3.1. Natural Seasonal and Spatial Variability

In order to provide context about how this simulation unfolds in the Bering Sea system we explore seasonal changes in TA, DIC, and pCO$_2$ at four simulated stations, or spatial checkpoints, across the Bering Sea (Figure 1, blue dots). These stations are presented and discussed in order of increasing distance from the TA addition location in Unimak Pass. The first analysis station, referred to as the adjusted Unimak Pass location, is located 60 km north of the TA addition site. We used this location rather than the actual release site due to the presence of oscillatory numerical artifacts in the immediate vicinity of the TA addition. The oscillatory artifacts are a well-studied phenomenon resulting from dispersive errors in the model's tracer advection scheme near sharp gradients (Gerdes et al., 1991; Shchepetkin & McWilliams, 1998), such as those imposed by our simple experimental design. Mass and tracers are conserved despite these artifacts and offsetting the analysis site avoids the impacts of artifacts on our simulated station records. The two stations at M2 (56.87°N, 164.05°W, Stabeno et al., 2016) and M5 (59.9°N, 171.7°W, Stabeno et al., 2016) were chosen because they are co-located with long term moored observing platforms along the 70 m isobath. Our final analysis station is in the Bering Strait, which is chosen to represent the northern boundary of the modeled Bering Sea.

The simulated carbonate chemistry exhibits considerable seasonal and spatial variability (Figure 2). The TA was higher in the warmer summer season (~2,250 μmol kg^{-1}) than in the windy colder season (2,200 μmol kg^{-1}) near Unimak Pass, while DIC and pCO$_2$ reaches minimum values of 2,000 μmol kg^{-1} and 200 μatm, respectively, in the summer months. Solubility-driven DIC fluxes should be anticorrelated with pCO$_2$ changes, so we attribute these correlated changes instead to strong biological removal, which also increases the surface summer pH and Ω (Figure 2e). The spring (March to May) and later summer (August to September) phytoplankton blooms lead to reductions in pCO$_2$ at both the M2 and M5 stations (Figures 2b and 2c). The seasonal amplitude is around
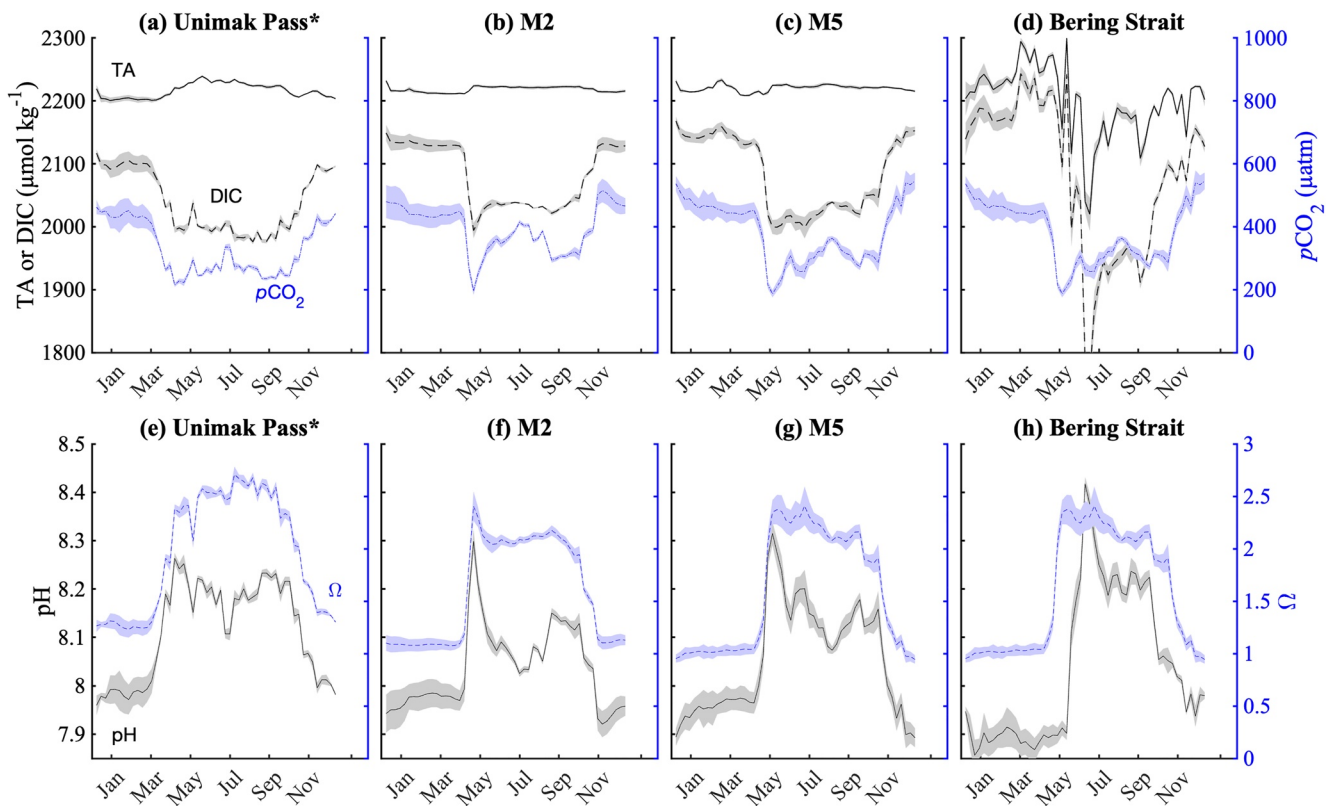
Figure 2. The natural seasonal and interannual variabilities of surface total alkalinity (TA) (black solid line), dissolved inorganic carbon (DIC) (black dashed line), and pCO$_2$ (blue line) from the control simulation near (at the location of the black circle in map inset) Unimak Pass (a, 60 km northwest of TA addition site indicated by the red circle), (b) M2 (56.87°N, 164.05°W), (c) M5 (59.9°N, 171.7°W), and (d) the Bering Strait. The bottom panels show the distribution of pH (black solid line) and Ω (the blue dashed line) in the same simulated stations (i.e., bounding model grid cells). The shaded areas show the standard deviation of each individual parameter based on 10 years of control simulation.

100 μmol kg^{-1} for DIC and 300 μatm for pCO$_2$ across the Bering shelf except in the Bering Strait. The pH and Ω (calcium carbonate saturation state) seasonal amplitudes are approximately 0.2 and 2, respectively. The carbonate chemistry shows larger fluctuations near the Bering Strait mainly resulting from the varied impacts from primary productivity, sea ice melting, and water mass mixing with the fresh and warm Alaska Coastal Water. The average salinity in the Bering Strait drops from 31.8 to 30.5 in the model simulation (data not shown here) due to mixing with this water mass. This amount of freshening would correspond to a TA reduction of 100 μmol kg^{-1} with a low-alkalinity freshwater endmember such as is expected from sea ice melt and Yukon river (Mathis et al., 2011), and this is close to the observed changes in the Bering Strait (50–150 μmol kg^{-1}, Figure 2d).

3.2. Temporal Variability of Surface OAE and Associated Carbonate Chemistry Changes

Due to the ~10 km spatial resolution of this model, our simulations do not adequately resolve the very local-scale impacts around the site of the TA addition. Furthermore, dispersive errors (not shown) created by the sharp TA gradients near the release site make the simulated changes in the immediate vicinity of the TA addition unreliable (though the changes are conserved in bulk). Instead, we consider changes on a regional scale, with the nearest example station being ~60 km northeast of the TA addition site (Figure 1a, map, black dot). At this station, the average surface TA′ of the 10-year simulation increases from ~1 μmol kg^{-1} in January to ~10 μmol kg^{-1} in June (blue lines in Figure 3a), and then TA′ slowly decreases to 1 μatm kg^{-1} in December. The temporal variability of surface TA′ at this location is dominated by the physical structure and seasonal shifts in the prevailing wind speed near Unimak Pass. The geostrophic water transport through Unimak Pass is positively correlated with the southwestward winds (Stabeno et al., 2002). The absolute geostrophic transport from October to April is about twice as much as that from May to September (Stabeno et al., 2016). Therefore, the slow water transport in the summer season is favorable for TA accumulation near Unimak Pass, while the faster advection in winter can
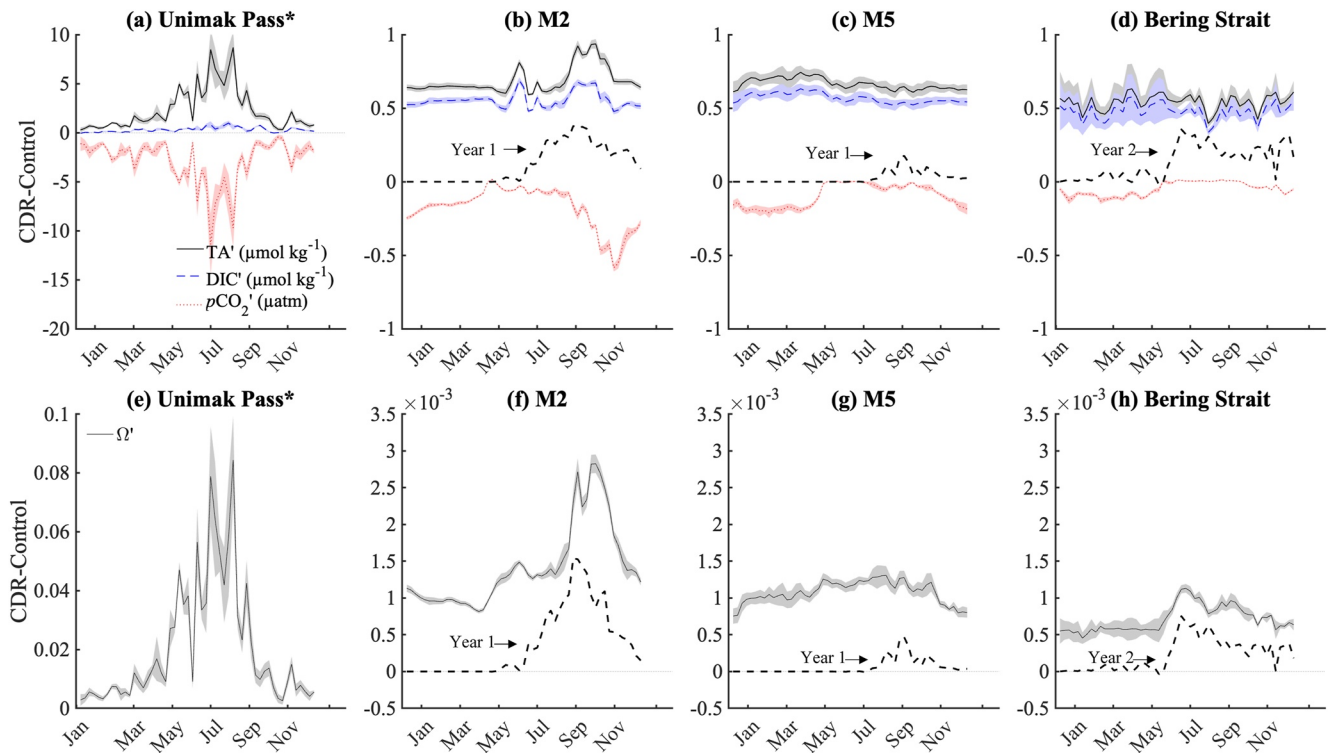
Figure 3. Seasonality of surface TA′ (solid black line), DIC′ (blue dashed line), and pCO_2′ (red dashed line) at the adjusted Unimak Pass (a), M2 (b), M5 (c), and Bering Strait (d) simulated stations. The bottom panels show the distribution of Ω′ in the same simulated stations. The lines with shaded areas in panels (a) and (e) show the averages and standard deviation from Year 1 to Year 10. The lines with shaded areas in panels (b, c, f, g) show the averages and standard deviations from Year 2 to Year 10, with TA′, DIC′, pCO_2′ (upper panel), and Ω′ (bottom panel) in Year 1 provided separately. The lines with shaded areas in panels (d) and (h) show the averages and standard deviation from Year 3 to Year 10 with TA′, DIC′, pCO_2′ (upper panel), and Ω′ (bottom panel). For discussion purposes the surface TA in Year 1 is highlighted with dashed lines for M2 and M5; the surface TA in Year 2 is highlighted with dashed lines for the Bering Strait (d, h). Individual years are separated from the averages displayed when it takes multiple years for the changes at an example station to approach steady state. Panels (a) and (e), being closer to the alkalinity addition location, reaches steady state sooner than the further panel, panels (d) and (h).

quickly spread the previously-accumulated TA across a wider area. The geostrophic transport through Unimak Pass is also related to the tidal cycle (Stabeno et al., 2002), and the tidal rectification may trap the ice meltwaters along the Bering Sea shelf (Kowalik & Stabeno, 1999). The high-frequency TA′ changes (Figure 3a) seem to match high-frequency variability in the control simulation TA (Figure 2a), suggesting that these features are related to the ephemeral flow pattern changes from sea ice formation/retreat and tidal changes and are not simply numerical artifacts.

The DIC′ value is dependent both on the TA′ and on the thermodynamics of sea-air exchange which are controlled by temperature, CO_2 conditions, and wind speed. The addition of TA reduces surface pCO_2 by up to 10 µatm or increases surface Ω up to 0.1 near Unimak Pass (Figure 3a). However, the surface DIC′ is always less than 1 µmol kg^{-1} near Unimak Pass, mainly because the water is advected away from the point of TA addition before the enhanced sea-air flux of CO_2 can meaningfully elevate the surface DIC. Theoretically, TA′ near Unimak Pass would produce a higher DIC′ at equilibrium with atmospheric CO_2. However, the water current near Unimak Pass is about 10 cm s^{-1} (Stabeno et al., 2016). The grid size in Unimak Pass is ~10 km, so it would only take about one day to fully replenish the mitigated water parcel compared to the ~months required for completed sea-air CO_2 equilibration. It takes about 5 months for the water with added alkalinity to reach the M2 station from Unimak Pass (Figures 3b and 3f), 7 months to reach the M5 mooring location (Figures 3c and 3g), and 12 months to reach the Bering Strait. This spin-up period is also present by the temporal evolution of TA, DIC, and pCO_2 at each location (Figure S1). Note, there are no carbonate chemistry changes in the first year near the Bering Strait. This time lag matches field observations that it takes a drifter released in Unimak Pass ~4 months to pass St. George Island and 13 months to reach the vicinity of St. Lawrence Island (Stabeno et al., 2016).
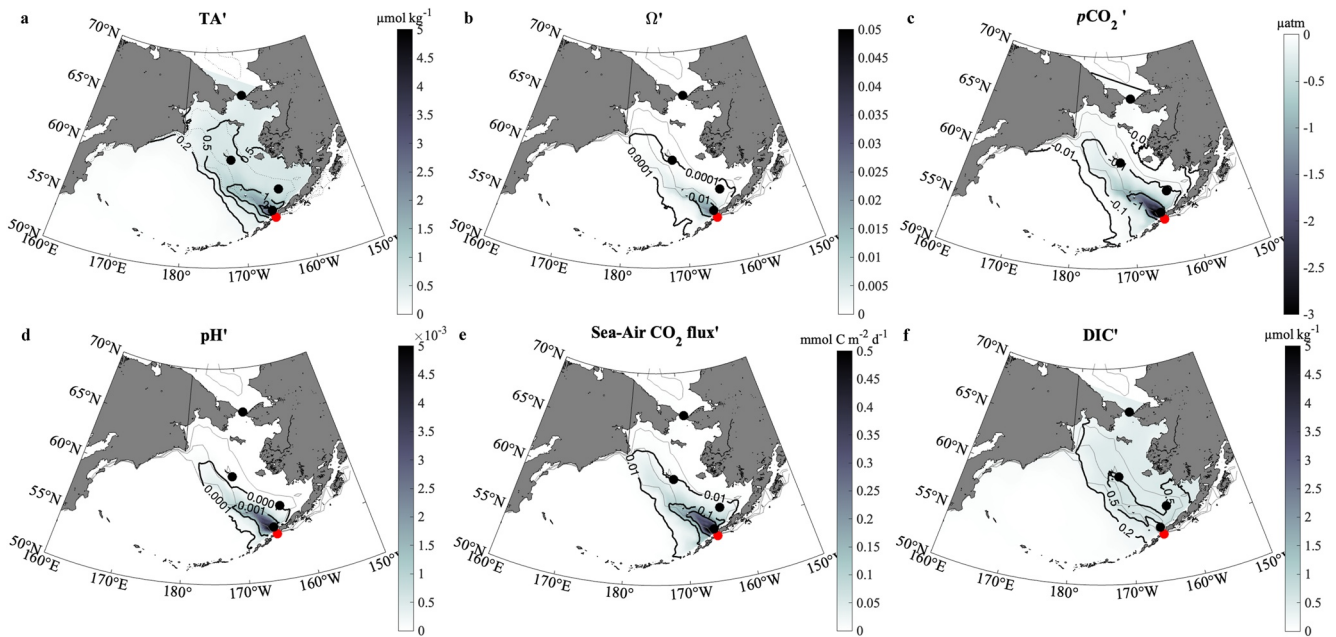
Figure 4. The surface distribution of TA′ in µmol kg^{-1} (a), Ω′ (b), pCO$_2$′ in µatm (c), pH′ (d), sea-air CO$_2$ flux anomaly in mmol m^{-2} d^{-1} (e), and DIC′ in µmol kg^{-1} (f) averaged over 10 simulated years after the commencement of alkalinity addition. The gray contour lines are bathymetric depths of 50 m, 100 m, and 250 m. The definition of " ′ " is the difference between experimental and control experiments. The results south of Unimak Pass suffer from the oscillatory artifacts mentioned previously, so results south of the Aleutian island arc are omitted from these maps. The black dots are the station locations from Figure 1 and the southeastern-most red dot corresponds to the Unimak Pass total alkalinity (TA) addition site.

With about a year of transport time or longer from Unimak Pass, the seawater reaching the Bering Strait has had ample time for sea-air CO$_2$ exchange. Therefore, the carbonate chemistry approaches complete equilibrium (with small average pCO$_2$′ and Ω in years 3+, Figure 3). The spatial and temporal changes of pCO$_2$′ and Ω′ also hold true of pH′, which is not shown here. To summarize, the seasonality of DIC′ and Ω reflects the transport time of TA′ from Unimak Pass to the various sites and the sea-air CO$_2$ exchanges that occur during transport.

3.3. Regional Patterns of Surface Ocean Carbonate Chemistry Changes From Alkalinity Enhancement

Most of the positive TA′ and DIC′ is found along the eastern Bering Sea shelf, where water depths are less than 250 m (Figure 4a). As noted in Section 2.2, TA′ is the direct result of alkalinity addition in Unimak Pass. Figure 4 demonstrates a key principle for OAE, which is that alkalinity elevation (Figure 4a) initially mitigates OA by increasing carbonate (e.g., Figure 4b) through the net reaction:

$$OH^- + HCO_3^- \Leftrightarrow H_2O + CO_3^{2-}$$
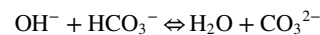
This rapidly changes pCO$_2$ (Figure 4c) and pH (Figure 4d) and increases the potential (Figure 5a) for enhanced sea-air CO$_2$ exchange (Figure 4e). This enhanced ocean CO$_2$ uptake balances the elevated TA with enhanced DIC (Figure 4d) through the net reaction:

$$CO_2 + CO_3^{2-} + H_2O \Leftrightarrow 2HCO_3^-$$
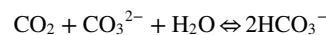
which restores pCO$_2$ and pH near their original values. Thus, Figures 4b, 4c, 4d and 4f show the OAE fingerprint for OA mitigation in this model domain whereas Figures 4e and 4f and Figure 5 show the OAE fingerprint for CDR. Due to rapid dilution of the TA′ through physical mixing, the unrealized CDR$_{potential}$ is >1 µmol kg^{-1} in the areas nearest the TA addition site (Figure 5b) with SAF$^+$/TA$^+$ in the surface layer of less than 0.1 in warm seasons. The mean surface TA′ is less than 2 µmol kg^{-1} across most of the model domain. Due to compensating DIC increases, this concentration of acid removal decreases the surface pCO$_2$ by less than 1 µatm (where pCO$_2$′ is negative, Figure 4c) except near Unimak Pass (Figures 3a and 4c) where the CDR potential is mostly unrealized (Figure 5b). The mean surface DIC increases <0.5 µmol kg^{-1} (Figure 4f) and the sea-air CO$_2$ flux increases
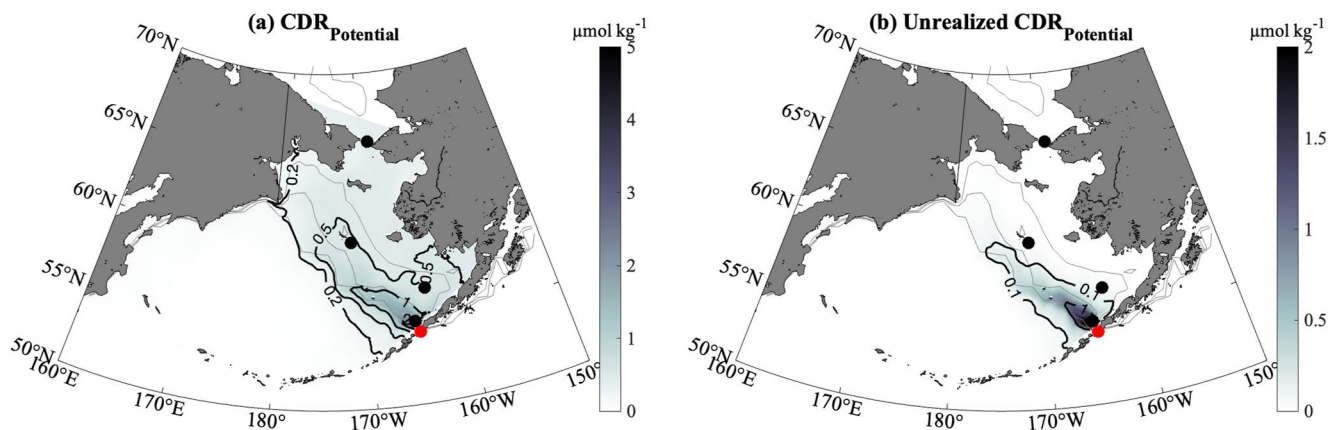
Figure 5. (a) The surface distribution of average carbon dioxide (CO_2) removal potential ($CDR_{Potential}$), the maximum dissolved inorganic carbon (DIC) increase expected due to ocean alkalinity enhancement (OAE), and (b) the "unrealized $CDR_{potential}$," that is, the difference between experimental DIC′ and expected DIC′ after air-sea gas exchange over the first 10 simulated years following total alkalinity (TA) addition. All units are µmol kg⁻¹. The gray contour lines show the 50 m, 100 m, and 250 m isobaths.

<0.2 mmol m⁻² d⁻¹ (Figure 4e). Figure 4a contours also show how the predominant flow exiting Unimak Pass travels northwest near the continental margin before redirecting north and exiting the model domain through the Bering Strait. Furthermore, the limited spatial extent of the elevated CO_2 flux anomaly plume highlights how most of the additional air-sea CO_2 exchange is complete well before the water mass exits the model domain. Relatedly, the $CDR_{potential}$ appears fully realized in the northern Bering Sea (Figure 5b).

The maximum DIC′ is less than 1 µmol kg⁻¹ across most of the model domain (Figure 4f), less than current observational measurement uncertainty. Similarly, all the pCO_2′ changes across the Bering Sea are less than 10 µatm (Figure 4c), which is less than half of the natural variability observed near Unimak Pass that cannot be removed through deseasonalization (27 µatm, Carter et al., 2019). Thus, even the largest of these signals would be difficult to separate from natural variability.

3.4. Time Series of Carbonate Chemistry Changes From TA Addition

If OAE is to be considered for its potential for OA mitigation as well as CDR, then maximizing the area of OA mitigation or habitat restoration is critical. In this context, here we explore the spatial extent over which pCO_2 is reduced. The blue line in Figure 6 shows that the area over which pCO_2 is reduced by >10 µatm (i.e., offsetting approximately 1/14th of the anthropogenic perturbation from CO_2 emissions to the atmosphere) varies seasonally
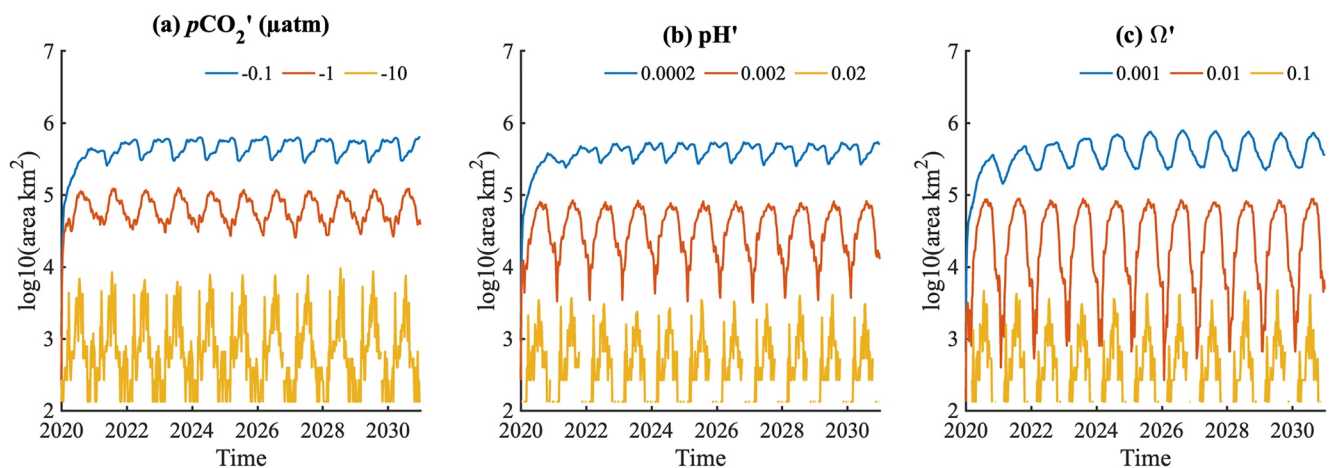

Figure 6. The area ranges of given thresholds: (a) pCO_2, (b) pH, and (c) Ω anomalies caused by point-source ocean alkalinity enhancement at a rate of 4 µmol m⁻² s⁻¹ in Unimak Pass, Bering Sea.

from just over 100 km^2 (equaling the approximate grid size of Unimak Pass addition site) in winter up to an area of 6,000 km^2 (i.e., 50 model grid cells) in summer (Section 3.3). These fluctuations are consistent with an accumulation of excess alkalinity in the vicinity of the intervention site that is episodically advected into the broader Bering Sea and then mixed across a broad region of the surface ocean. For more minor pCO_2 perturbations (0.5 µatm), the signal is mixed across a much larger area (~100,000 km^2). The smallest perturbations (e.g., a pCO_2 decrease of 0.01 µatm) are felt across much of the ~6 M km^2 model domain. The pH and aragonite saturation changes follow the same spatial pattern as for pCO_2: the aragonite saturation increases by about 0.1 near the mitigation site, while the rest of the Bering shelf only increases between 0.001 and 0.01; these threshold values of 0.1, 0.01, and 0.001 for aragonite saturation show similar seasonality in area affected as seen for the 10, 0.5, and 0.01 µatm pCO_2 thresholds, respectively. The pH increases by less than 0.02 near and beyond the intervention site while the Bering Sea only slightly increases its pH on average between 0.0002 and 0.002, which is less than the precision of most timeseries pH measurements.

Figure 6 shows that meaningful OA mitigation can only be achieved from OAE in the vicinity of a TA addition. However, it also demonstrates how the plume of elevated TA can be rapidly diluted across a broad region of the surface ocean. This dilution suggests that monitoring the impacts of OAE in the open ocean will be challenging: small mitigation signals (see Figure 5) will become lost amid the large natural variability in the ocean carbonate system (see Figure 2) (Carter et al., 2019). To overcome this limitation, monitoring efforts aimed at quantifying the impacts of TA addition will likely be limited to the immediate vicinities of the TA addition sites. Figure 6 shows that scaling a single point-source intervention to a sufficient magnitude to make a measurable impact over a large area would result in very large impacts on local scales (Renforth & Henderson, 2017), especially when considering that the largest impacts would occur on finer spatial scales than are adequately resolved by our simulations. Adding TA mitigates OA to a point, but very large additions could raise local pH and Ω beyond preindustrial conditions and thereby potentially create new ecosystem stress or risk inorganic mineral precipitation. Rather, an array of moderate OAE interventions dispersed throughout a region or a diffuse TA addition approach (e.g., operating on shipping vessels, e.g., Butenschön et al., 2021; Mongin et al., 2021) would likely be required to minimize the acute impacts at the point of addition. Additional higher-resolution modeling work is needed to constrain the magnitude of impacts at the point of TA addition.

3.5. Vertical Distribution of Alkalinity Enhancement

We also examined the vertical extent of the elevated TA plume. This is crucial to quantify whether OAE can achieve the desired effects on the timescales of years to decades. If the added TA were mixed into the subsurface layer too quickly then the water mass would not have enough time to absorb atmospheric CO_2. Our simulations show that in the Bering Sea the rate at which added TA mixes into the subsurface is significantly less than the rate at which it equilibrates with atmospheric CO_2. As a result, the shallow seasonal mixed-layer depth (<50 m, Hermann et al., 2016) and weak vertical turbulent mixing permit the accumulation of TA′ at the surface. At its simplest, the Bering Sea's impacted water column can be treated as a single well-mixed box. The average area across the 10-year simulation where TA′ is ≥0.5 µmol kg^{-1} is 688,000 km^2. If all the added TA only extended across this area, the penetration depth equals 49 m. This depth is consistent with the plume of elevated simulated TA visible along a transect near the southern edge of the Bering Sea shelf (Figure 7), implying that, indeed, most of the added TA remains near the ocean surface within the modeled domain. The unrealized CDR$_{potential}$ is less than 1 µmol kg^{-1} everywhere except immediately adjacent to Unimak Pass; the unrealized CDR$_{potential}$ below 20 m is less than 0.5 µmol kg^{-1} at all locations (Figure 7c).

3.6. Seasonality in the Water Column DIC′/TA′

Both TA and DIC only started to increase near the Bering Strait (66°N, 191°E. Figure 3d) in December of Year 1, so it is safe to conclude that it would take about 1 year for the leading edge of the mitigated water parcel to be advected across the Bering Sea. As noted, the TA′ within the basin can only be attributed to the TA addition in Unimak Pass. The basin-wide water column integrated TA′ increases almost linearly throughout the first year and at the end of first year is 1.64 × 10^{10} mol, which is slightly less than the added TA (1.67 × 10^{10} mol yr^{-1}) in Unimak Pass. The small discrepancy can be attributed to advection of the TA plume through the open boundaries of the model domain, primarily through the Bering Strait (Figure 4d). DIC′ increases nonlinearly in the first year
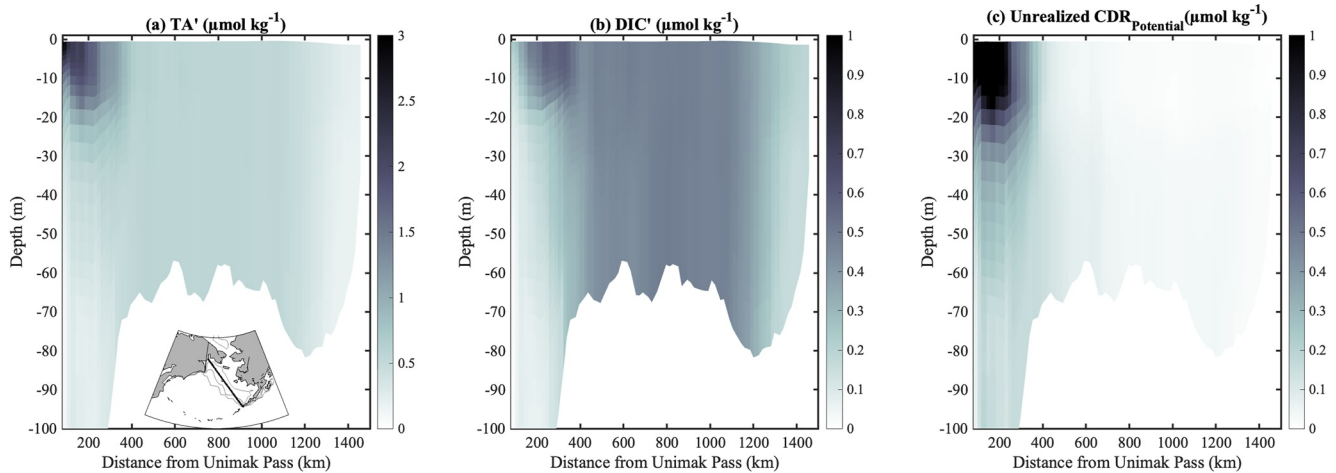
Figure 7. The vertical distribution of mean (a) TA′, (b) DIC′, and (c) unrealized CDR$_{Potential}$ in example transects (the insert panel in the left corner) across the 10-year model simulations. The left side of these plots is the side closest to Unimak Pass.

and reaches 1.09×10^{10} mol yr^{-1} at the end of Year 1 (Figure 8). The DIC′ lags the increase in TA′ due to the limited sea-air exchange rate.

An interesting feature can be seen in the water column DIC′/TA′, particularly after the model reaches steady state (Figure 8). After Year 6 the TA′ appears nearly constant, yet the DIC′ develops a distinct seasonal cycle with higher values in the winter and lower values in the summer. These differences are too pronounced to be attributable to seasonality in Northern Hemisphere atmospheric CO$_2$, and are instead related to variations in the expected DIC′/TA′ at equilibrium. Seasonality in the seawater properties results in an ~8% decrease in this ratio between winter and summer months (not shown). Seasonality in the expected DIC′ due to shifts in seawater properties (i.e., warming) can be seen in the tendency for pCO$_2$′ to approach 0 during the warmer summer months even when there is an approximately constant TA′ source (Figures 3b and 3c). In each of these cases, the warming summer conditions reduce the CDR potential for a given TA′ (~8%). The seasonality highlights how the water column DIC′/TA′ can continue to vary even after the initial TA addition is fully equilibrated. Presumably, the calculated CDR$_{potential}$ would continue to vary until the water is subducted into the ocean interior.

Figure 8. The integrated water column TA′ (in blue) and DIC′ (in red) inside the model domain from Year 1 (yr 1) to Year 10 (yr 10). The vertical line highlighted the changes at the end of Year 1.

3.7. CDR Efficiency and Limitations of Regional Models for Local-Scale OAE Impact Modeling

There is a maximum SAF$^+$/TA$^+$ achieved at complete sea-air CO$_2$ equilibration that varies depending on the temperature and initial chemical concentrations of the perturbed water (Burt et al., 2021). The integrated sea-air CO$_2$ flux over the first year is 1.12×10^{10} mol yr^{-1} (Figure 8). After several years our SAF$^+$/TA$^+$ is higher than the values from previous biogeochemical models in other regions (0.71–0.84, Burt et al., 2021), due to both the high bulk DIC:TA ratio in the Bering Sea and the mitigated seawater staying near the surface (<50 m) within the modeled domain. This is consistent with the relatively strong alkalinity sensitivity, that is, the change in seawater pCO$_2$ per molar increase of TA (γAlk = $\partial \ln p$CO$_2$/∂ lnAlk, Sarmiento & Gruber, 2006), found in the Bering Sea. A more negative alkalinity sensitivity implies a stronger reduction in the pCO$_2$ and a greater sensitivity to OAE. The typical alkalinity sensitivity in the surface ocean is −9.4, meaning that pCO$_2$ decreases by about 9.4% when alkalinity is increased by 1%. However, because of the naturally-high DIC and TA in the Bering Sea, the alkalinity sensitivity in most of the Bering Sea ranges from −15 to −12, which is more
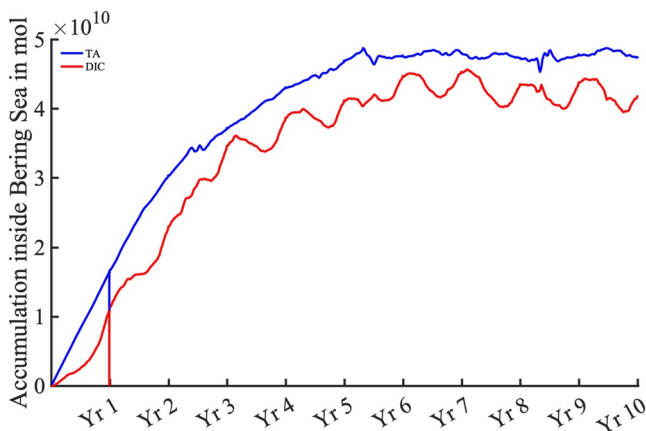
Table 1
The Mass Balance Budget Related to Ocean Alkalinity Enhancement in the Bering Sea Over the 10 Years of the Simulation

	Total TA addition	Air-sea flux′	Integrated DIC flux		Annual average DIC′	CDR$_{Potential}$	
	(10^{10} mol)	(10^5 Metric ton CO_2 yr^{-1})	(10^5 Metric ton CO_2)	SAF$^+$/TA$^+$	(10^5 Metric ton CO_2)	(10^5 Metric ton CO_2)	Carbon-uptake efficiency
Year 1	1.67	4.94	4.94	0.67	1.50	3.26	0.46
Year 2	3.34	6.39	11.33	0.77	7.17	9.59	0.75
Year 3	5.01	6.59	17.92	0.81	12.41	13.69	0.91
Year 4	6.68	6.32	24.23	0.82	15.49	16.11	0.96
Year 5	8.35	6.43	30.67	0.83	17.08	18.04	0.95
Year 6	10.02	6.47	37.14	0.84	18.31	19.23	0.95
Year 7	11.69	6.43	43.56	0.85	19.19	19.45	0.99
Year 8	13.36	6.41	49.98	0.85	18.79	19.28	0.97
Year 9	15.03	6.21	56.18	0.85	18.48	19.14	0.97
Year 10	16.7	6.47	62.65	0.85	18.53	19.45	0.95

Note. Total TA (total alkalinity) addition is calculated based on a fixed annual TA addition rate 1.67×10^{10} mol yr^{-1}. The integrated dissolved inorganic carbon (DIC) flux is the summary of annual sea-air CO_2 flux anomaly for all previous years. SAF$^+$/TA$^+$ is as defined in Section 2.2. The carbon-uptake efficiency is the ratio between the annual average DIC′ and the CDR$_{potential}$ at complete equilibration with the added TA. The definition of " ′ " is the difference between experimental and control simulations.

negative than the global mean (−9.4). Therefore, it follows that the SAF$^+$/TA$^+$ in the Bering Sea would also be higher.

It takes more than 3 years for TA′ and DIC′ values to reach a steady state within our domain (Figure 8). The domain-wide CDR efficiency climbs from 0.46 to 0.91 between the first and third years, and averages 0.96 (±0.01 standard deviation) for all subsequent years (Table 1). This value gets close to "1" but never reaches it, which we attribute primarily to the continued addition of TA throughout the simulation (and thus at all times there is TA that has just been added and has had no time to equilibrate). The steady state efficiency is comparable (0.97 ± 0.01) when calculated using the atmospheric pCO$_2$ in the efficiency calculation in place of the in situ pCO$_2$ (data not shown). The steady state CDR efficiency (Table 1) after the first 3 years implies that the model is near steady state with respect to sea-air exchange and boundary DIC′ loss after this timespan, consistent with the stabilization of changes seen after 3 years in Figure 3d. In subsequent years, the TA′ and DIC′ accumulation curves plateau as the TA addition in Unimak Pass and the DIC′ from enhanced sea-air exchange are balanced by lateral transports out of the Bering Strait (Figure 8). We speculate that the efficiency would climb closer still to 1 if the simulated TA addition stopped and model simulation continued, but we did not test this scenario.

Previous studies have shown that the SAF$^+$/TA$^+$ decreases over time with continued TA addition (Burt et al., 2021). This is because OAE tends to decrease the DIC to TA ratio. This feedback can partially explain why previous modeling studies with larger TA additions (e.g., 70–700 µmol kg^{-1}) and longer simulations (e.g., 75 years) found a smaller SAF$^+$/TA$^+$ ratio (which is equivalent to the DIC′ to TA′ ratio in global models). We note that this feedback is not thoroughly explored in our regional model of the Bering Sea because of our short (10 years) simulation, our modest TA addition, and because added TA is lost when it is exported across the model domain's open boundaries.

While the high SAF$^+$/TA$^+$ and CDR efficiency support the notion that the Bering Sea would be an ideal candidate for OAE, it should be pointed out that the effects of increasing alkalinity can continue to vary even after CO_2 is removed from the atmosphere. Notably, water exiting the Bering Sea with high DIC can later outgas a portion of the anomalous accumulated DIC when the thermodynamic properties of that water are altered by warming, evaporation, or biogeochemical cycling. Ultimately, what matters for CDR is how much additional carbon remains in the seawater when it next enters the ocean interior and loses contact with the atmosphere on the timescales relevant for carbon cycle management. This is an important difference between global modeling efforts that account for all CO_2 exchanges and our regional model which does not account for any changes that occur outside of the modeled domain. This distinction will need to be considered when using modeling as a support tool for CDR

measurement, reporting, and verification. Therefore our 0.85 steady state SAF$^+$/TA $^+$ ratio cannot be directly compared to the global values of previous studies. Our short OAE simulation here is therefore suitable for testing immediate mitigation of atmospheric CO_2 removal rate but not the long-term response of ocean carbonate chemistry. Nevertheless, the high SAF$^+$/TA$^+$ and CDR efficiency we find suggests that the Bering Sea would not suffer from the efficiency losses expected when surface waters are entrained into interior water masses before the sea-air CO_2 re-equilibration following TA addition. We speculate that the CDR efficiency would remain close to 1 when the seawater with excess TA exits our model domain, while the SAF$^+$/TA$^+$ would decline slightly in response to natural degassing of elevated biologically-accumulated DIC in the poorly-buffered Bering Sea. However, testing this speculation would require a longer simulation with a global model with well-validated deep and intermediate water mass formation processes.

3.8. Timescale of Re-Equilibration Following TA Addition

The near-unity efficiency value after Year 3 implies that most of the CDR potential from the TA′ is realized within the modeled domain, as does the nearly complete equilibration observed in the northern Bering Sea both at the surface (Figure 5) and at depth (Figure 7). If we assume the unrealized CDR$_{potential}$ remaining from incomplete net air-to-sea CO_2 exchange is in steady state with its creation rate (R_{CDR}) through TA′ additions within Unimak pass, then we can calculate an approximate rate constant for the re-equilibration of CO_2 following OAE. It follows from gas-exchange kinetics that the sea-air exchange rate should be roughly proportional to the magnitude of the disequilibrium—or the amount of unrealized CDR$_{potential}$ remaining within the domain. Wind speeds are also important for air-sea exchange, but our repeating wind forcing and steady TA addition rate suggests all years are equivalent in this regard. Thus the rate of removal can be approximated as $k*$(unrealized CDR$_{potential}$), where k is the rate constant with units of yr^{-1}. The rate of removal should equal the known rate of TA′ addition at Unimak Pass multiplied by a conversion factor to relate TA′ to CDR$_{potential}$, which we assume to average ∼0.9 based on Section 3.7. Dividing this product by the steady state unrealized CDR$_{potential}$ for years 6–10 of 0.15×10^{10} mol DIC (derived from Table 1) results in a k value of ∼10 yr^{-1}. This implies an e-folding timescale ($1/k$) of ∼5 weeks for the sea-air-exchange-induced reduction of the unrealized CDR$_{potential}$ created through TA addition in Unimak Pass. This suggests that CDR resulting from TA added in Unimak pass would be >95% complete after ∼3.6 months. This is within the range of CO_2 equilibration timescales found by Jones et al. (2014).

4. Conclusions and Implications

The simulated OAE in the Bering Sea shows a high carbon-uptake efficiency (96%) and a higher-than-typically-reported ratio of simulated CDR impact for a given TA addition (0.85 here as a lower bound after 3 years vs. 0.71–0.84 as given by Burt et al. (2021)) which we attribute in part to the shallow water column depth and relatively high regional background value of water column DIC/TA. Our regional model simulation shows that sustained point-source OAE in Bering Sea could remove CO_2 and partially mitigate OA in the vicinity of the TA addition. The high efficiency within this regional domain and short 10-year simulation suggests that most of the enhanced ocean CO_2 uptake occurs locally and on comparatively rapid timescales relative to the 10–100 years timescales needed for climate interventions by the end of the century. We also show that the expected CDR impact changes seasonally with changes in seawater properties.

With the high CDR efficiency and CDR impact ratio, an addition of 1.67×10^{10} mol TA yr^{-1} or 667,950 metric tons yr^{-1} of NaOH, in Unimak Pass would be expected to result in 639,905 tons of additional CO_2 storage in the ocean. Even with this high impact, it would take >8,000 of these TA addition interventions operating by the year 2100 to meet the 5.5 Gt CO_2 yr^{-1} target that the IPCC suggested could be needed to stabilize global warming at 1.5°C (and likely more as others have found the CDR impact ratio tends to decrease as the amount of TA added increases). This study gives us no reason to doubt that electrochemical OAE can be a powerful tool to help the world meet its carbon removal and OA mitigation targets, but it should be one tool among many that we assess, develop, and potentially deploy at scale over the coming decades to address the challenges posed by legacy and future CO_2 emissions.

This regional model simulation is aimed at resolving the regional spatial scales of point-source OAE impacts, and we argue that the Bering10K model is adequate for this purpose. The most meaningful pCO_2 decreases (10 µatm)

are localized in the 100–100,000 km^2 around the addition region, highlighting the meaningful oceanic changes near the alkalinity addition areas.

Extensive research has been conducted to understand the impact of OA by increasing pCO$_2$ and/or decreasing pH and Ω on marine biota. However, there are few studies investigating the impact of reverting OA or elevated TA on marine biota and global carbon cycle (Renforth & Henderson, 2017). Furthermore, the ecosystem impacts of OAE are not well understood, and it remains to be demonstrated whether OAE would have positive or harmful impacts on ocean ecosystems. We show that the larger TA changes near the TA addition site consume CO$_2$ from local seawater without immediate replenishment through sea air CO$_2$ exchange (Figure S1). Accordingly, the changes have the potential to affect the marine biota. Additionally, the rapid increase of CO$_3^{2-}$ may trigger secondary precipitation of CaCO$_3$, which reduces the atmospheric CO$_2$ uptake (Hartmann et al., 2022; Moras et al., 2021). However, in this study, most pCO$_2$ changes in OAE-impacted areas were less than 0.5 µatm, and the small average changes found far from the addition site should have limited impact on marine biota.

The small changes found far from the intervention site pose a challenge for monitoring the impacts of an OAE implementation on carbon cycling: by the time the sea-air CO$_2$ exchange is complete, the DIC′ will be small and diffuse signal over a very broad area. The precision for current commercially available pCO$_2$ and DIC instruments is around ±2 µatm and ±2 µmol kg^{-1}, respectively. In this study we would only expect to be able to detect the signals from OAE in TA, pH, and pCO$_2$ in the immediate vicinity of the TA addition site, particularly when considering the significant natural variability in these variables.

A strength of our regional modeling approach—relative to a lower resolution global circulation model—is the ability to resolve higher resolution processes and features in the CDR response. We note four limitations of our regional model approach, however. First, a regional model cannot capture the changes in the SAF$^+$/TA$^+$ that occur after the seawater advects outside of the regional domain and before it becomes entrained into the ocean interior. Similarly, our regional model cannot account for feedbacks upon the boundary conditions that occur when the global domain is meaningfully changed by the modeled process (without nesting the model). Third, we do not model feedbacks between carbonate mineral cycling and seawater carbonate chemistry, and it is possible that elevated TA could encourage TA loss through biotic carbonate mineral precipitation, particularly in the area around the TA addition where the impacts are greatest. Finally, no model can resolve processes acting on finer spatial scales than the spatial resolution of the model, so while the regional Bering10K model is more highly-resolved than most global-scale models, it still fails to resolve some of the most acute local-scale impacts from a localized TA addition. This highlights the need for OAE modeling across a range of spatial scales.

Data Availability Statement

The source code used for the simulations in this paper (encompassing the ROMS regional ocean model and BEST_NPZ biogeochemical model) is available on GitHub at https://github.com/beringnpz/roms-bering-sea; a snapshot of the specific release used (K20P19) is archived under https://doi.org/10.5281/zenodo.7062782. Selected output from the two simulations—including all temperature, salinity, and carbonate system output—is available through Zenodo at https://doi.org/10.5281/zenodo.7065495. Data saved in the hd5 format for Figures 2–8 have been archived to Zenodo: https://10.5281/zenodo.7058878. Requests for specific subsets of model output will be honored whenever possible at the cost of data transmission.

References

Aagaard, K., Weingartner, T. J., Danielson, S. L., Woodgate, R. A., Johnson, G. C., & Whitledge, T. E. (2006). Some controls on flow and salinity in Bering Strait. *Geophysical Research Letters*, *33*(19), 1–5. https://doi.org/10.1029/2006GL026612

Bednaršek, N., Naish, K. A., Feely, R. A., Hauri, C., Kimoto, K., Hermann, A. J., et al. (2021). Integrated assessment of ocean acidification risks to pteropods in the northern high latitudes: Regional comparison of exposure, sensitivity and adaptive capacity. *Frontiers in Marine Science*, *8*(September), 1–23. https://doi.org/10.3389/fmars.2021.671497

Burt, D. J., Fröb, F., & Ilyina, T. (2021). The sensitivity of the marine carbonate system to regional ocean alkalinity enhancement. *Frontiers in Climate*, *3*(July), 1–15. https://doi.org/10.3389/fclim.2021.624075

Butenschön, M., Lovato, T., Masina, S., Caserini, S., & Grosso, M. (2021). Alkalinization scenarios in the Mediterranean sea for efficient removal of atmospheric CO$_2$ and the mitigation of ocean acidification. *Frontiers in Climate*, *3*, 614537. https://doi.org/10.3389/fclim.2021.614537

Caldeira, K., & Rau, G. H. (2000). Accelerating carbonate dissolution to sequester carbon dioxide in the ocean: Geochemical implications. *Geophysical Research Letters*, *27*(2), 225–228. https://doi.org/10.1029/1999GL002364

Carter, B. R., Williams, N. L., Evans, W., Fassbender, A. J., Barbero, L., Hauri, C., et al. (2019). Time of detection as a metric for prioritizing between climate observation quality, frequency, and duration. *Geophysical Research Letters*, *46*(7), 3853–3861. https://doi.org/10.1029/2018GL080773

Cross, J. N., Mathis, J. T., Bates, N. R., & Byrne, R. H. (2013). Conservative and non-conservative variations of total alkalinity on the southeastern Bering Sea shelf. *Marine Chemistry*, *154*, 100–112. https://doi.org/10.1016/j.marchem.2013.05.012

Cross, J. N., Mathis, J. T., Lomas, M. W., Moran, S. B., Baumann, M. S., Shull, D. H., et al. (2014). Integrated assessment of the carbon budget in the southeastern Bering Sea. *Deep-Sea Research Part II Topical Studies in Oceanography*, *109*, 112–124. https://doi.org/10.1016/j.dsr2.2014.03.003

Cross, J. N., Mathis, J. T., Pickart, R. S., & Bates, N. R. (2018). Formation and transport of corrosive water in the Pacific Arctic region. *Deep-Sea Research Part II Topical Studies in Oceanography*, *152*(June), 67–81. https://doi.org/10.1016/j.dsr2.2018.05.020

de Lannoy, C.-F., Eisaman, M. D., Jose, A., Karnitz, S. D., DeVaul, R. W., Hannun, K., & Rivest, J. L. B. (2018). Indirect ocean capture of atmospheric CO_2: Part I. Prototype of a negative emissions technology. *International Journal of Greenhouse Gas Control*, *70*, 243–253. https://doi.org/10.1016/j.ijggc.2017.10.007

Doney, S. C., Busch, D. S., Cooley, S. R., & Kroeker, K. J. (2020). The impacts of ocean acidification on marine ecosystems and reliant human communities. *Annual Review of Environment and Resources*, *45*(1), 83–112. https://doi.org/10.1146/annurev-environ-012320-083019

Eisaman, M. D. (2020). Negative emissions technologies: The tradeoffs of air-capture economics. *Joule*, 516–520. https://doi.org/10.1016/j.joule.2020.02.007

Eisaman, M. D., Parajuly, K., Tuganov, A., Eldershaw, C., Chang, N., & Littau, K. (2012). CO_2 extraction from seawater using bipolar membrane electrodialysis. *Energy & Environmental Science*, *5*(6), 7346. https://doi.org/10.1039/C2EE03393C

Eisaman, M. D., Rivest, J. L. B., Karnitz, S. D., de Lannoy, C.-F., Jose, A., DeVaul, R. W., & Hannun, K. (2018). Indirect ocean capture of atmospheric CO_2: Part II. Understanding the cost of negative emissions. *International Journal of Greenhouse Gas Control*, *70*, 254–261. https://doi.org/10.1016/j.ijggc.2018.02.020

Falkowski, P., Scholes, R. J., Boyle, E., Canadell, J., Canfield, D., Elser, J., et al. (2000). The global carbon cycle: A test of our knowledge of Earth as a system. *Science*, *290*(5490), 291–296. https://doi.org/10.1126/science.290.5490.291

Ferrer-González, M., & Ilyina, T. (2016). Impacts of artificial ocean alkalinization on the carbon cycle and climate in Earth system simulations. *Geophysical Research Letters*, *43*(12), 6493–6502. https://doi.org/10.1002/2016GL068576

Friedlingstein, P., O'Sullivan, M., Jones, M. W., Andrew, R. M., Hauck, J., Olsen, A., et al. (2020). Global carbon budget 2020. *Earth System Science Data*, *12*(4), 3269–3340. https://doi.org/10.5194/essd-12-3269-2020

Gerdes, R., Köberle, C., & Willebrand, J. (1991). The influence of numerical advection schemes on the results of ocean general circulation models. *Climate Dynamics*, *5*(4), 211–226. https://doi.org/10.1007/BF00210006

Gibson, G. A., & Spitz, Y. H. (2011). Impacts of biological parameterization, initial conditions, and environmental forcing on parameter sensitivity and uncertainty in a marine ecosystem model for the Bering Sea. *Journal of Marine Systems*, *88*(2), 214–231. https://doi.org/10.1016/j.jmarsys.2011.04.008

Grear, J. S., Rynearson, T. A., Montalbano, A. L., Govenar, B., & Menden-Deuer, S. (2017). pCO₂ effects on species composition and growth of an estuarine phytoplankton community. *Estuarine, Coastal and Shelf Science*, *190*, 40–49. https://doi.org/10.1016/j.ecss.2017.03.016

Haidvogel, D. B., Arango, H., Budgell, W. P., Cornuelle, B. D., Curchitser, E., Di Lorenzo, E., et al. (2008). Ocean forecasting in terrain-following coordinates: Formulation and skill assessment of the Regional Ocean modeling system. *Journal of Computational Physics*, *227*(7), 3595–3624. https://doi.org/10.1016/j.jcp.2007.06.016

Hamilton, J. L., Wilson, S. A., Morgan, B., Harrison, A. L., Turvey, C. C., Paterson, D. J., et al. (2020). Accelerating mineral carbonation in ultramafic mine tailings via direct CO_2 reaction and heap leaching with potential for base metal enrichment and recovery. *Economic Geology*, *115*(2), 303–323. https://doi.org/10.5382/econgeo.4710

Hartmann, J., Suitner, N., Lim, C., Schneider, J., & Marín-samper, L. (2022). Stability of alkalinity in Ocean Alkalinity Enhancement (OAE) approaches—Consequences for durability of CO_2 storage (pp. 1–29). https://doi.org/10.5194/bg-2022-126

Harvey, L. D. D. (2008). Mitigating the atmospheric CO_2 increase and ocean acidification by adding limestone powder to upwelling regions. *Journal of Geophysical Research*, *113*(C4), C04028. https://doi.org/10.1029/2007jc004373

Hermann, A. J., Gibson, G. A., Bond, N. A., Curchitser, E. N., Hedstrom, K., Cheng, W., et al. (2016). Projected future biophysical states of the Bering Sea. *Deep-Sea Research Part II Topical Studies in Oceanography*, *134*, 30–47. https://doi.org/10.1016/j.dsr2.2015.11.001

Hunt, G. L., & Stabeno, P. J. (2002). Climate change and the control of energy flow in the southeastern Bering Sea. *Progress in Oceanography*, *55*(1–2 SPEC ISS.), 5–22. https://doi.org/10.1016/S0079-6611(02)00067-8

Ilyina, T., Wolf-Gladow, D., Munhoven, G., & Heinze, C. (2013). Assessing the potential of calcium-based artificial ocean alkalinization to mitigate rising atmospheric CO_2 and ocean acidification. *Geophysical Research Letters*, *40*(22), 5909–5914. https://doi.org/10.1002/2013GL057981

IPCC. (2022). Climate change 2022: Mitigation of climate change. In P. R. Shukla, J. Skea, R. Slade, A. Al Khourdajie, R. van Diemen, D. McCollum, et al. (Eds.), *Contribution of Working Group III to the Sixth Assessment Report of the Intergovernmental Panel on Climate Change*. Cambridge University Press. https://doi.org/10.1017/9781009157926

Jones, D. C., Ito, T., Takano, Y., & Hsu, C.-W. (2014). Spatial and seasonal variability of the air-sea equilibration timescale of carbon dioxide. *Global Biogeochemical Cycles*, *28*(11), 1163–1178. https://doi.org/10.1002/2014GB004813

Kearney, K., Hermann, A., Cheng, W., Ortiz, I., & Aydin, K. (2020). A coupled pelagic-benthic-sympagic biogeochemical model for the Bering Sea: Documentation and validation of the BESTNPZ model (v2019.08.23) within a high-resolution regional ocean model. *Geoscientific Model Development*, *13*(2), 597–650. https://doi.org/10.5194/gmd-13-597-2020

Kearney, K. A., Alexander, M., Aydin, K., Cheng, W., Hermann, A. J., Hervieux, G., & Ortiz, I. (2021). Seasonal predictability of sea ice and bottom temperature across the eastern Bering Sea shelf. *Journal of Geophysical Research: Oceans*, *126*(11), 1–21. https://doi.org/10.1029/2021JC017545

Kelemen, P., Benson, S. M., Pilorgé, H., Psarras, P., & Wilcox, J. (2019). An overview of the status and challenges of CO_2 storage in minerals and geological formations. *Frontiers in Climate*, *1*, 9. https://doi.org/10.3389/fclim.2019.00009

Keller, D., Feng, E., & Oschlies, A. (2014). Potential climate engineering effectiveness and side effects during a high carbon dioxide-emission scenario. *Nature Communications*, *5*(1), 3304. https://doi.org/10.1038/ncomms4304

Kheshgi, H. S. (1995). Sequestering atmospheric carbon dioxide by increasing ocean alkalinity. *Energy*, *20*(9), 915–922. https://doi.org/10.1016/0360-5442(95)00035-f

Kleypas, J. A., Seibel, B. A., & Feely, R. A. (2019). *Impacts of ocean acidification on marine biodiversity*. In Biodiversity and climate change: Transforming the Biosphere (pp. 185–195). https://doi.org/10.2307/j.ctv8jnzw1.25

Köhler, P., Hartmann, J., & Wolf-Gladrow, D. A. (2010). Geoengineering potential of artificially enhanced silicate weathering of olivine. *Proceedings of the National Academy of Sciences of the United States of America*, *107*(47), 20228–20233. https://doi.org/10.1073/pnas.1000545107

Kowalik, Z., & Stabeno, P. (1999). Trapped motion around the Pribilof islands in the Bering Sea. *Journal of Geophysical Research*, *104*(C11), 25667–25684. https://doi.org/10.1029/1999JC900209

Lewis, E. R., & Wallace, D. W. R. (1998). *Program developed for CO2 system calculations. Rep. BNL-61827*. U.S. Dep. of Energy, Oak Ridge Natl. Lab., Carbon Dioxide Inf. Anal. Cent.

Mathis, J. T., Cross, J. N., & Bates, N. R. (2011). Coupling primary production and terrestrial runoff to ocean acidification and carbonate mineral suppression in the eastern Bering Sea. *Journal of Geophysical Research*, *116*(C2), C02030. https://doi.org/10.1029/2010JC006453

Meseck, S. L., Sennefelder, G., Krisak, M., & Wikfors, G. H. (2020). Physiological feeding rates and cilia suppression in blue mussels (*Mytilus edulis*) with increased levels of dissolved carbon dioxide. *Ecological Indicators*, *117*(July), 106675. https://doi.org/10.1016/j.ecolind.2020.106675

Mongin, M., Baird, M. E., Lenton, A., Neill, C., & Akl, L. (2021). Reversing ocean acidification along the Great Barrier Reef using alkalinity injection. *Environmental Research Letters*, *16*(6), 064068. https://doi.org/10.1088/1748-9326/ac002d

Moras, C. A., Bach, L. T., Cyronak, T., Joannes-Boyau, R., & Schulz, K. G. (2021). Ocean Alkalinity Enhancement – Avoiding runaway $CaCO_3$ precipitation during quick and hydrated lime dissolution. *Biogeosciences Discussions*(December), 1–31. https://doi.org/10.5194/bg-2021-330

National Academies of Sciences, Engineering, and Medicine. (2021). *A research strategy for ocean-based carbon dioxide removal and sequestration*. The National Academies Press. https://doi.org/10.17226/26278

Orr, J. C., Fabry, V. J., Aumont, O., Bopp, L., Doney, S. C., Feely, R. A., et al. (2005). Anthropogenic ocean acidification over the twenty-first century and its impact on calcifying organisms. *Nature*, *437*(7059), 681–686. https://doi.org/10.1038/nature04095

Orr, J. C., Najjar, R., Sabine, C. L., & Joos, F. (1999). Abiotic-HOWTO. Internal OCMIP report (p. 25). Retrieved from https://www.cgd.ucar.edu/oce/OCMIP/HOWTO-Abiotic.pdf

Perotto, G., Ceseracciu, L., Simonutti, R., Paul, U. C., Guzman-Puyol, S., Tran, T.-N., et al., (2018). Bioplastics from vegetable waste via an eco-friendly water-based process. *Green Chemistry*, *20*(4), 894–902. https://doi.org/10.1039/c7gc03368k

Pilcher, D. J., Naiman, D. M., Cross, J. N., Hermann, A. J., Siedlecki, S. A., Gibson, G. A., & Mathis, J. T. (2019). Modeled effect of coastal biogeochemical processes, climate variability, and ocean acidification on aragonite saturation state in the Bering Sea. *Frontiers in Marine Science*, *5*(Jan), 1–18. https://doi.org/10.3389/fmars.2018.00508

Qi, Y. (2021). The neutralization and recycling of red mud – A review. *Journal of Physics: Conference Series*, *1759*, 012004. https://doi.org/10.1088/1742-6596/1759/1/012004

Rau, G. H. (2008). Electrochemical splitting of calcium carbonate to increase solution alkalinity: Implications for mitigation of carbon dioxide and ocean acidity. *Environmental Science & Technology*, *42*(23), 8935–8940. https://doi.org/10.1021/es800366q

Rau, G. H. (2011). CO_2 mitigation via capture and chemical conversion in seawater. *Environmental Science & Technology*, *45*(3), 1088–1092. https://doi.org/10.1021/es102671x

Rau, G. H., & Caldeira, K. (1999). Enhanced carbonate dissolution: A means of sequestering waste CO_2 as ocean bicarbonate. *Energy Conversion and Management*, *40*(17), 1803–1813. https://doi.org/10.1016/S0196-8904(99)00071-0

Rau, G. H., Carroll, S. A., Bourcier, W. L., Singleton, M. J., Smith, M. M., & Aines, R. D. (2013). Direct electrolytic dissolution of silicate minerals for air CO_2 mitigation and carbon-negative H_2 production. *Proceedings of the National Academy of Sciences of the United States of America*, *110*(25), 10095–10100. https://doi.org/10.1073/pnas.1222358110

Renforth, P., & Henderson, G. (2017). Assessing ocean alkalinity for carbon sequestration. *Reviews of Geophysics*, *55*(3), 636–674. https://doi.org/10.1002/2016RG000533

Sabatino, F., Mehta, M., Grimm, A., Gazzani, M., Gallucci, F., Kramer, J. G., & Annaland, M. v. (2020). Evaluation of a direct air capture process combining wet scrubbing and bipolar membrane electrodialysis. *Industrial & Engineering Chemistry Research*, *59*(15), 7007–7020. https://doi.org/10.1021/acs.iecr.9b05641

Saha, S., Moorthi, S., Wu, X., Wang, J., Nadiga, S., Tripp, P., et al. (2010). The NCEP climate forecast system reanalysis. *Bulletin of the American Meteorological Society*, *91*(8), 1015–1057. https://doi.org/10.1175/2010BAMS3001.1

Sarmiento, J. L., & Gruber, N. (2006). *Ocean biogeochemical dynamics*. Princeton University Press.

Schorr, M., Valdez, B., Zlatev, R., & Stoytcheva, M. (2010). Phosphate ore processing for phosphoric acid production: Classical and novel technology. *Mineral Processing and Extractive Metallurgy*, *119*(3), 125–129. https://doi.org/10.1179/174328509X481882

Schuiling, R. D., & Krijgsman, P. (2006). Enhanced weathering: An effective and cheap tool to sequester CO_2. *Climate Change*, *74*(1–3), 349–354. https://doi.org/10.1007/s10584-005-3485-y

Scott, A., Oze, C., Shah, V., Yang, N., Shanks, B., Cheeseman, C., et al. (2021). Transformation of abundant magnesium silicate minerals for enhanced CO_2 sequestration. *Communications Earth & Environment*, *2*(1), 25. https://doi.org/10.1038/s43247-021-00099-6

Shchepetkin, A. F., & McWilliams, J. C. (1998). Quasi-monotone advection schemes based on explicit locally adaptive dissipation. *Monthly Weather Review*, *126*(6), 1541–1580. https://doi.org/10.1175/1520-0493(1998)126<1541:QMASBO>2.0.CO;2

Shchepetkin, A. F., & McWilliams, J. C. (2005). The regional oceanic modeling system (ROMS): A split-explicit, free-surface, topography-following-coordinate oceanic model. *Ocean Modelling*, *9*(4), 347–404. https://doi.org/10.1016/j.ocemod.2004.08.002

Stabeno, P. J., Danielson, S. L., Kachel, D. G., Kachel, N. B., & Mordy, C. W. (2016). Currents and transport on the Eastern Bering Sea shelf: An integration of over 20 years of data. *Deep-Sea Research Part II Topical Studies in Oceanography*, 134, 13–29. https://doi.org/10.1016/j.dsr2.2016.05.010

Stabeno, P. J., Reed, R. K., & Napp, J. M. (2002). Transport through Unimak Pass, Alaska. *Deep-Sea Research Part II Topical Studies in Oceanography*, *49*(26), 5919–5930. https://doi.org/10.1016/S0967-0645(02)00326-0

Wanninkhof, R. (2014). Relationship between wind speed and gas exchange over the ocean revisited. *Limnology and Oceanography: Methods*, *12*(June), 351–362. https://doi.org/10.4319/lom.2014.12.351

Woodgate, R. A., & Aagaard, K. (2005). Revising the Bering Strait fresh-water flux into the Arctic ocean. *Geophysical Research Letters*, *32*(2), 1–4. https://doi.org/10.1029/2004GL021747